Supplementary information: High precision detection of change in intermediate range order of amorphous zirconia-doped tantala thin films due to annealing

K. Prasai,[1,*] J. Jiang,[2] A. Mishkin,[2] B. Shyam,[3] S. Angelova,[4] R. Birney,[4] D. A. Drabold,[5] M. Fazio,[6] E. K. Gustafson,[7] G. Harry,[8] S. Hoback,[8] J. Hough,[9] C. Lévesque,[10] I. MacLaren,[9] A. Markosyan,[1] I. W. Martin,[9] C. S. Menoni,[6] P. G. Murray,[9] S. Penn,[11] S. Reid,[4] R. Robie,[9] S. Rowan,[9] F. Schiettekatte,[10] R. Shink,[10] A. Turner,[9] G. Vajente,[7] H-P. Cheng,[2] M. M. Fejer,[1] A. Mehta,[12] and R. Bassiri[1,†]

[1] *E. L. Ginzton Laboratory, Stanford University, Stanford, California 94305, USA*
[2] *Department of Physics and Quantum Theory Project, University of Florida, Gainesville, Florida 32611, USA*
[3] *University of Dayton Research Institute, Dayton, Ohio 45469, USA*
[4] *SUPA, Department of Biomedical Engineering, University of Strathclyde, Glasgow G1 1QE, United Kingdom*
[5] *Department of Physics and Astronomy, Ohio University, Athens, Ohio 45701, USA*
[6] *Department of Electrical and Computer Engineering, Colorado State University, Fort Collins, Colorado 80523, USA*
[7] *LIGO Laboratory, California Institute of Technology, Pasadena, California 91125, USA*
[8] *Department of Physics, American University, Washington, DC 20016, USA*
[9] *SUPA, School of Physics and Astronomy, University of Glasgow, Glasgow G12 8QQ, UK*
[10] *Department of Physics, Université de Montréal, Québec H3T 1J4, Canada*
[11] *Department of Physics, Hobart and William Smith Colleges, Geneva, New York 14456, USA*
[12] *SLAC National Accelerator Laboratory, Menlo Park, California 94025, USA*

(Dated: May 25, 2019)

S1. Motivations for studying zirconia-doped tantala

The work presented in this letter is a part of research directed at identifying low Brownian thermal noise optical coatings for the test masses of the LIGO gravitational wave detectors. The current generation of the LIGO detectors use highly reflective dielectric coatings for its core-optics, which consist of alternating layers of amorphous silica and titania-doped-tantala. At the most sensitive frequency range (~ 40 - 200 Hz), these coatings give rise to a limit in the detector sensitivity due to Brownian thermal noise. The dominant source of Brownian thermal noise arises from the mechanical loss in the high-refractive index titania-doped-tantala layers, with a mechanical loss of $\sim 2 \times 10^{-4}$.

The current coatings for LIGO optics are deposited using ion-beam sputtering (IBS). One of the ways of reducing the thermal noise at room temperature of thin film coatings is post-deposition annealing [1]. For the case of zirconia-doped tantala studied in this work, room-temperature mechanical loss shows steady decrease as a function of post-deposition annealing temperature.

The mechanical loss was measured at room temperature as a function of post-deposition annealing temperature from two separate coatings runs for similar coatings used for GIPDF analysis of zirconia-doped tantala ($\mathrm{Zr/(Ta+Zr)} \simeq 0.48$) coatings. The results shown in figure 1 indicate that, as with pure tantala, the mechanical loss of zirconia-doped tantala decreases with increasing post-deposition annealing temperature. As indicated in figure 1, the annealing time is extended for temperatures at 600°C and above, but appears to have little effect at 600°C compared to the annealing temperature. Interestingly, the 800°C annealed sample has a loss of 1.8×10^{-4} that is slightly below the currently employed titania-doped tantala coatings, and demonstrates that zirconia-doped tantala is a promising coating material system that warrants further study as a potential Advanced LIGO + coating.

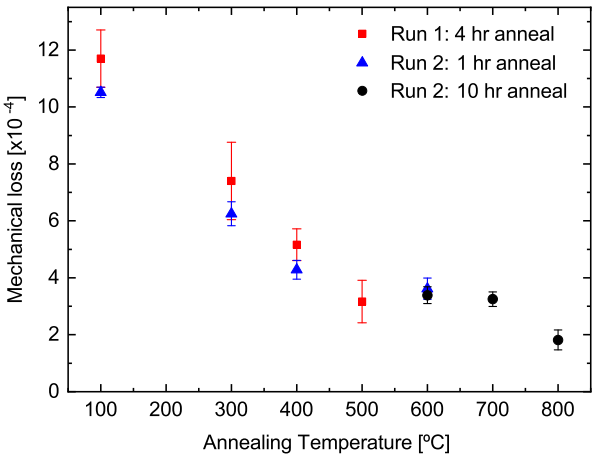

FIG. 1. Mechanical loss at room temperature for zirconia doped tantala as a function of annealing temperature. The substrates used were silica cantilevers for Run 1 and 75 mm diameter silica discs for Run 2, the details of the measurement process are described in Ref. [2].

S2. Density and composition of samples

We measured the composition, density and thickness of two of the four samples used in GIPDF measurements. Those two samples are as-deposited and 800°C annealed. The composition was determined using Rutherford Backscattering Spectrometry (RBS) [3] analysis where the samples were exposed to a beam of α particles at an energy of 2.9 MeV at normal incidence and the back-scattered particles were detected at 170°. Atomic concentrations were determined by fitting a simulated spectra to the measured spectra. The best fit was obtained at the concentrations given in table I.

TABLE I. **Composition measurements using RBS**

	Atomic Concentration (%)	
Element	**As deposited**	**800°C annealed**
Ta	16.00±0.15	15.50±0.15
Zr	14.8±0.3	14.8±0.3
O	66.4±1.5	67.0±1.5
Ar	2.8±0.4	2.7±0.4

Areal densities of the samples were also obtained from RBS to be 4370±90 × 10^{15} atoms/cm^2 for both as-deposited and 800°C annealed samples. The thicknesses of the samples were measured, using combinations of stylus profilometry and ellipsometry [4, 5] measurements, to be 589±4 nm and 587±10 nm for as-deposited and 800°C annealed samples respectively. Thickness measurements, combined with areal density and composition measurements from RBS, enabled us to calculate mass densities of the samples to be 6.53±0.15 gm/cm^3 for as-deposited sample and 6.53±0.18 gm/cm^3 for 800°C sample.

Following these measurements, we used a stoichiometric ratio of 15:67.5:15 for Ta, O and Zr respectively for all our models. We have not included Ar atoms in our models because the x-ray scattering signature of ∼2.5% Ar is low (see figure 2) and because our separate DFT based calculations (not shown here) indicate that Ar atoms have a negligible effect on the structure of the material itself. We used a density of 6.53 gm/cm^3 for our models, but we did take into account a mass of 2.5% Ar to obtain the effective box-size for our models. After considering the mass of Ar atoms, the effective density in our models is 6.41 gm/cm^3. The size of our models is chosen to enable computation of G(r) up to 15 Å which is the distance up to which measured GIPDF shows some degree of IRO. With all of these considerations in place, our final models have 400 Ta, 1800 O and 400 Zr in a cubic box of dimension 32.92 Å.

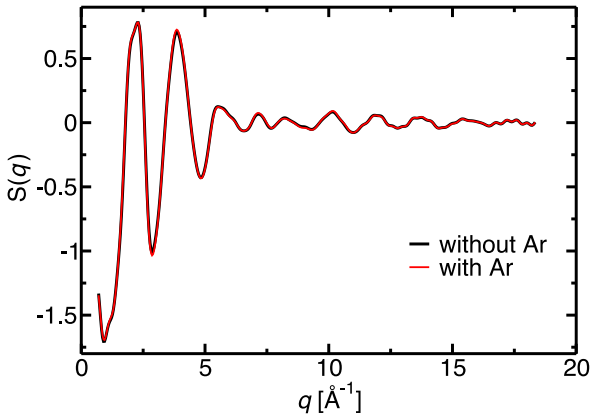

FIG. 2. The x-ray structure factors, S(q), computed from the models. The red curve is from a model which has Ta, O, Zr and Ar atoms in the ratio 15:67.5:15:2.5. The black curve represents when the Ar atoms were removed from the model.

S3. Integrated modeling approach

The modeling scheme that is used to obtain the atomic models presented in this work seeks to use all *a priori* information about the samples in order to generate realistic structural solutions. In this case, the set of *a priori* information consisted of density-functional-theory-based atomic models, a classical two-body force field, density and composition measurements on thin films, and the GIPDF S(q) data. These data are used to guide an RMC-based high-throughput modeling routine. In order to have the correct atomic ratio and supercell size in our models, we measured the composition and density in our samples using Rutherford Back-scattering Spectrometry (RBS) and used the results to constrain the composition and density of the models (see [6]). The measured PDFs show some structure up to a distance of ∼ 15 Å and accordingly the supercell size of the model is chosen to be able to compute G(r) up to 15 Å. Using the composition and density from the RBS measurements, we generated starting configurations of zirconia-doped tantala by employing melt-quench molecular dynamics (MD) simulations where we used two-body empirical potentials from [7, 8].

The flowchart in figure 3(a) shows the sequence of steps followed to obtain the final models. The modeling algorithm starts by considering 1000 independent systems where each system has 2600 randomly positioned atoms in a cubic supercell; a threshold distance of 1.9 Å between is maintained between the atoms even for random positions. The atomic ratio and density are chosen as discussed in section S2 and are kept fixed. These models are taken through a conventional melt-quench MD modeling cycle (as discussed in section S5). The final configurations from MD serve as the starting configuration for the RMC models. RMC moves are set to fit to the measured S(q) and are constrained by enforcing a distance window

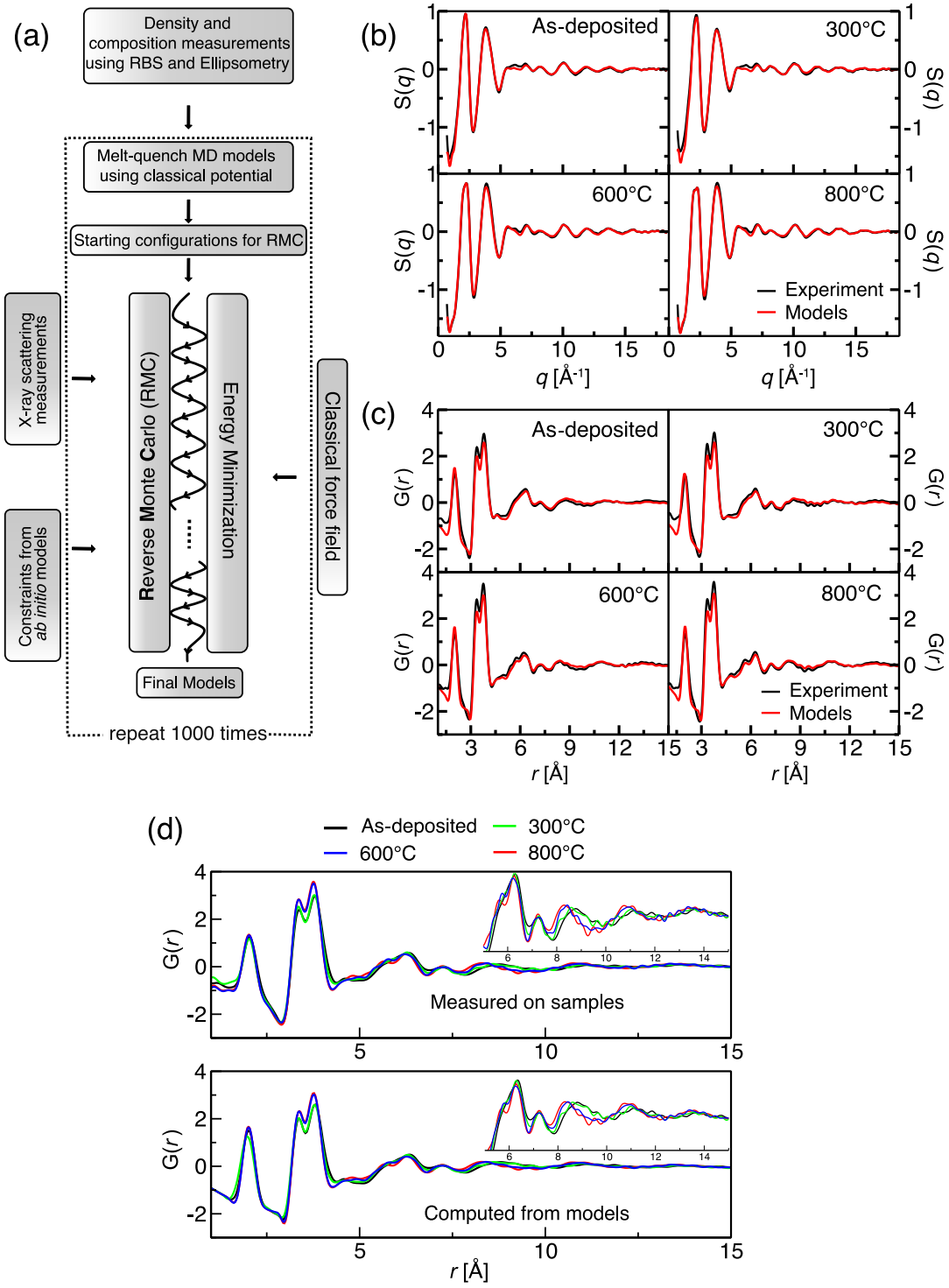

FIG. 3. **More on the modeling approach and results** (a) The integrated modeling approach: Illustration of how *ab initio* MD, classical MD, RMC based on measure GIPDF data and density and composition measurements of thin films are combined together to obtain models that are realistic and sensitive to annealing induced changes in the structure. (b) Goodness of fit: The structure factor, S(q), measured on samples is compared the corresponding fitted models. The computed S(q) are averages over 1000 models. (c) The computed G(r) on models are compared with G(r) obtained from GIPDF measurements. The computed G(r) are averages over 1000 models. (d) The ability of the computed models to track the changes in IRO seen in the measured G(r) at different annealing temperature. This figure is the complete version of figure 2 in main paper.

of 1.5 Å to 2.9 Å for Ta-O bond distance and of 1.5 Å to 3.2 Å for Zr-O bond distance. M-M lower cutoff of 2.9 Å and O-O lower cutoff of 2.0 Å were also used to constrain the RMC moves. These distances correspond to the lower and upper cutoff of the corresponding partial PDFs of AIMD-based models (see discussion in section S4 and figure 5). RMC moves and energy minimization moves are iterated back and forth until a convergence in chi-squared (degree of misfit) and a convergence in the total energy are reached. This iterative approach was first proposed as force enhanced atomic relaxation (FEAR) in [9, 10]. The final models from this process are considered as representative of the samples on which the GIPDF measurements were made. To get a better statistical accuracy, we repeat the process for 1000 independent models and take an average for all quantities reported in the paper. The plot of the fitted structure factor (S(q)) and the corresponding plot in real space is presented in figure 3(b) and (c).

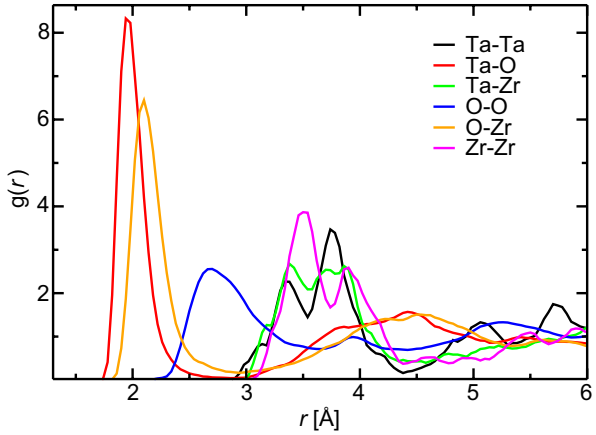

FIG. 5. The partial G(r) computed on AIMD models. Note that the definition of G(r) used in this plot is different the definition of G(r) used in the paper. In this case, $g_{\alpha\beta} = \frac{V}{4\pi r^2 N_\alpha}\frac{dn_{\alpha\beta}}{dr}$, where V is volume of supercell, N_α is number of species α, and $dn_{\alpha\beta}$ is the number of β atoms at distance r to $r+dr$ from α atom. This definition of G(r) is useful to help infer the cutoffs for atomic correlations. Additionally, the area under the partial G(r) give the corresponding coordinations as a function of r.

S4. Melt-quench models using *ab initio* molecular dynamics (AIMD)

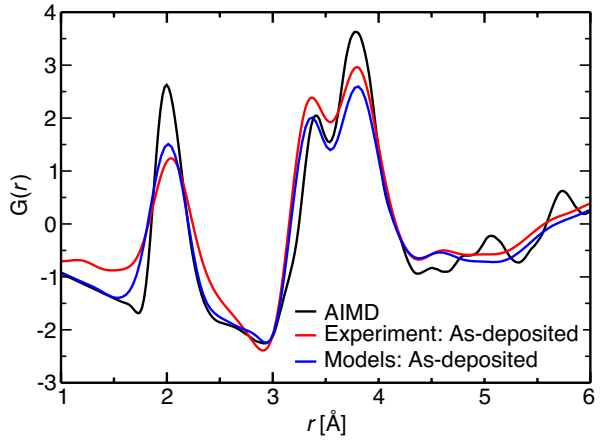

FIG. 4. The total G(r) of AIMD models is compared with measured G(r) and the computed G(r) from RMC based models.

We performed *ab initio* molecular dynamics (AIMD) to obtain smaller atomic models of zirconia-doped tantala. The purpose of this exercise was to provide geometrical constraints to bond distances during RMC modeling and also to enable basic sanity checks on our main models. 30 Ta atoms, 30 Zr atoms and 135 O atoms are taken in a cubic supercell of dimensions 13.78 Å and periodic boundary conditions were applied. This is equivalent to a bulk mass density of 6.55 gm/cm^3. In order to create the starting configuration for AIMD, the system is first taken through a melt-quench molecular dynamics cycle employing an empirical force field [7, 8] over a total time period of 1.15 ns. LAMMPS simulation software was used [11]. The starting configuration obtained is then taken through an AIMD melt-quench cycle using Vienna *ab initio* software package (VASP) [12, 13]. PBE functionals were used [14, 15] and valence electrons were treated using plane waves of upto 400 eV. The system was equilibrated at 4000 K, then at 2500 K, then quenched to 300 K, and then again equilibrated at 300 K. Total simulation time for the melt-quench dynamics was 104.6 ps, wherein time steps of 2 fs were used throughout the simulation. The computed G(r) from AIMD models is compared with measured G(r) and computed G(r) from RMC-based models in figure 4.

S5. Melt-quench models using classical molecular dynamics (CMD)

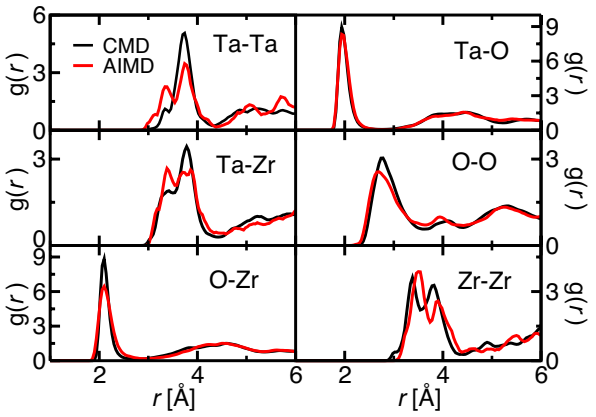

FIG. 6. Partial PDF from MD models: The partial PDFs obtained from the melt-quench MD modeling described in section S4 and S5 are plotted here for comparison. CMD denotes the models using classical molecular dynamics as described in section S5. AIMD denotes the *ab initio* molecular dynamics described in section S4. The partial PDFs from CMD are averages of 1000 snapshots of the model over 100 ps of MD at 300 K; each model contains 975 atoms. The partial PDFs from AIMD are averages of 7844 snapshots of the model over 15.7 ps of MD at 300 K; each model contains 195 atoms.

We use a unified classical two-body potential from references [7, 8] to perform the energy minimization component of our modeling (see figure 3). To investigate the ability of the potential to predict basic structural features, we carried out melt-quench molecular dynamics simulation in the framework of the classical potential. We used the LAMMPS simulation program [11] as follows: A random collection of 975 atoms (of type Ta, O and Zr atoms in the ratio discussed in section S2) in a supercell of size determined by the density is taken. Constant pressure (NPT) MD simulations were carried out at various starting densities (viz 6.0, 6.3, 6.55, 6.7, 7.0 and 7.5 gm/cm^3). For all simulations, the system was taken to a high temperature of 6000 K, equilibrated at that temperature, then cooled down to 300 K and equilibrated again at 300 K. The total number of steps was more than 1.3 $\times 10^6$ which corresponds to more than 1.3 ns of simulated time. The structures were finally relaxed to its minimum energy configurations using conjugate gradient algorithm. The final density of all the models converged to $\sim$6.8 gm/cm^3. In figure 6, we compare the partial PDFs of these models with the AIMD generated models (described in section S4). We find that the CMD predicts the basic features of the partial PDF correctly, although the M-M correlations are not predicted very well. The energy minimization with respect to the referenced force-field is a useful constraint, however one needs to be careful about how it interferes with the overall models. Note that the melt-quench MD used to generate the starting configurations for RMC modeling follows the same routine as described in this section, except that those models contain 2600 atoms and constant volume (NVT) ensemble is used for MD.

S6. Further plots on coordinations and bond angle distributions

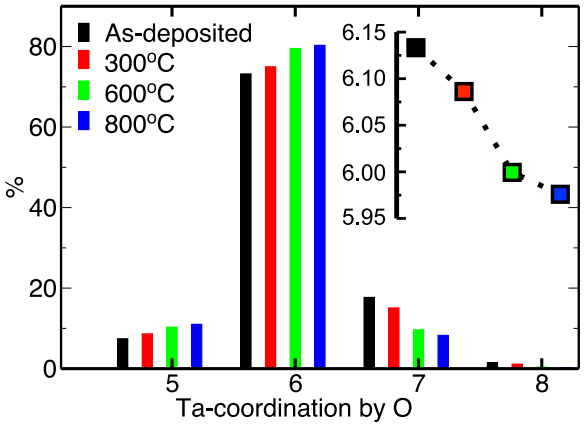

FIG. 7. The distribution of Ta-coordination by O atoms in our models. The bond cutoff is taken to be 2.90 Å which is the first minimum of total G(r). The coordination values are averages over 1000 models. The inset shows the average coordination number for the four samples.

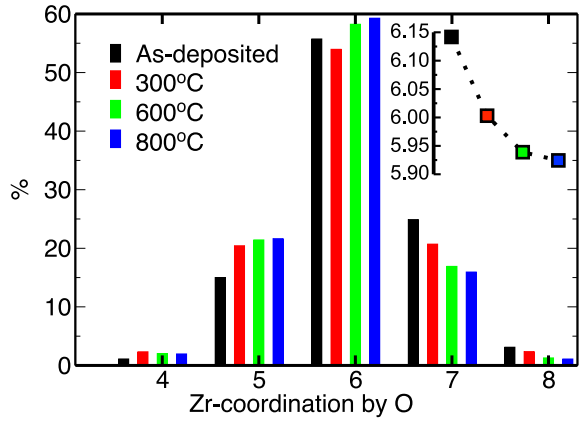

FIG. 8. The distribution of Zr-coordination by O atoms in our models. The bond cutoff is taken to be 2.90 Å which is the first minimum of total G(r). The coordination values are averages over 1000 models. The inset shows the average coordination number for the four samples.

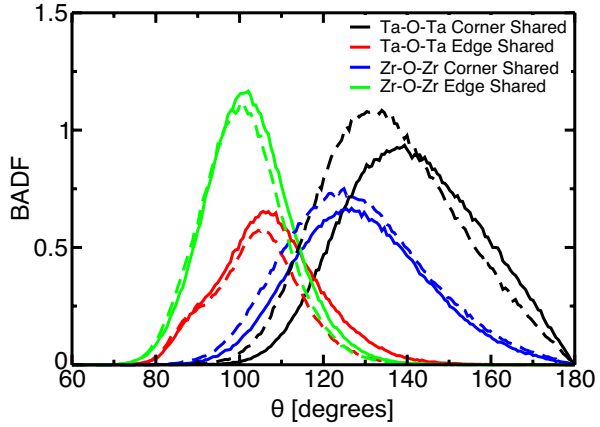

FIG. 9. BADF resolved into edge-sharing and corner-sharing polyhedra for Ta-O-Ta and Zr-O-Zr. Solid line represents as deposited sample and dashed line represents 800°C annealed sample.

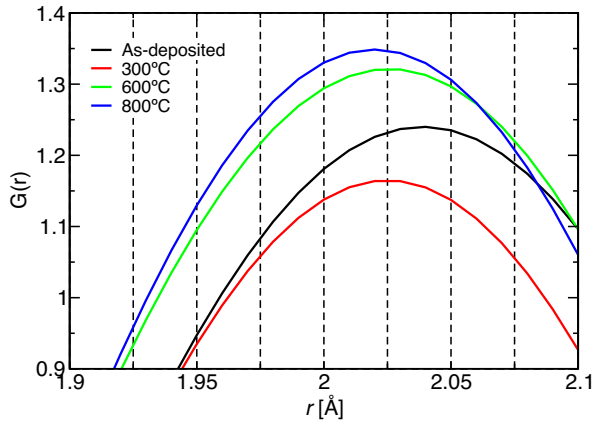

FIG. 10. The first peak in G(r) in high resolution. The positions of first peak correspond to M-O bond lengths.

* prasai@stanford.edu
† rbassiri@stanford.edu

[1] I. W. Martin, R. Bassiri, R. Nawrodt, M. Fejer, A. Gretarsson, E. Gustafson, G. Harry, J. Hough, I. MacLaren, S. Penn, *et al.*, Classical and Quantum Gravity **27**, 225020 (2010).
[2] G. Vajente, R. Birney, A. Ananyeva, S. Angelova, R. Asselin, B. Baloukas, R. Bassiri, G. Billingsley, M. Fejer, D. Gibson, *et al.*, Classical and Quantum Gravity **35**, 075001 (2018).
[3] W.-K. Chu, *Backscattering spectrometry* (Elsevier, 2012).
[4] A. Piegari and E. Masetti, Thin solid films **124**, 249 (1985).
[5] H. Fujiwara, *Spectroscopic ellipsometry: principles and applications* (John Wiley & Sons, 2007).
[6] See supplementary information for additional information on the simulation method and further numerical results.
[7] J. Trinastic, R. Hamdan, Y. Wu, L. Zhang, and H.-P. Cheng, The Journal of Chemical Physics **139**, 154506 (2013).
[8] J. Yu, R. Devanathan, and W. J. Weber, Journal of Materials Chemistry **19**, 3923 (2009).
[9] A. Pandey, P. Biswas, and D. A. Drabold, Scientific Reports **6**, 33731 (2016).
[10] A. Pandey, P. Biswas, and D. Drabold, Physical Review B **92**, 155205 (2015).
[11] S. Plimpton, Journal of Computational Physics **117**, 1 (1995).
[12] G. Kresse and J. Hafner, Physical Review B **47**, 558 (1993).
[13] G. Kresse and J. Furthmüller, Physical Review B **54**, 11169 (1996).
[14] P. E. Blöchl, Physical Review B **50**, 17953 (1994).
[15] J. P. Perdew, K. Burke, and M. Ernzerhof, Physical Review Letters **77**, 3865 (1996).